Upper Limb Tremors Classification for Parkinson's Disease Patients Using W-Band (76–81 GHz) Doppler Millimeter-Wave Sensing and a Deep Learning-Based Classifier

Pi-Yun Chen *, Chun-Yu Lin, Neng-Sheng Pai, Ping-Tzan Huang, Chao-Lin Kuo, Chien-Ming Li, Chia-Hung Lin *

Posted Date: 29 April 2026

doi: 10.20944/preprints202604.2032.v1

Keywords: Parkinson's disease; upper limb tremor (ULT); micro-Doppler effect (mDE); point cloud map; short-range and contactless; time-frequency transform (TFT); convolutional neural network (CNN)

 doi:10.20944/preprints202604.2032.v1

Article

Upper Limb Tremors Classification for Parkinson's Disease Patients Using W-Band (76–81 GHz) Doppler Millimeter-Wave Sensing and a Deep Learning-Based Classifier

Pi-Yun Chen [1,*], Chun-Yu Lin [1], Neng-Sheng Pai [1], Ping-Tzan Huang [2] and Chao-Lin Kuo [3], Chien-Ming Li [4] and Chia-Hung Lin [1,*]

[1] Department of Electrical Engineering, National Chin-Yi University of Technology, Taichung City, 41170, Taiwan

[2] Department of Biomechatronics Engineering, National Pingtung University of Science and Technology, Pingtung, 91201, Taiwan

[3] Department of Maritime Information and Technology, National Kaohsiung University of Science and Technology, Kaohsiung City, 80543, Taiwan

[4] Chien-Ming Li is with the Tainan Municipal Hospital, Infectious Disease Division of Internal Medicine Department, Tainan City, 701, Taiwan

* Correspondence: chenby@ncut.edu.tw (P.-Y.C.); eechl53@gmail.com (C.-H.L.)

Abstract

Parkinson's disease (PD) is a neurodegenerative disorder with an increasing incidence, significantly affecting patients' motor functions and quality of life. Involuntary upper limb tremor (ULT) commonly manifests unilaterally, affecting either the left or right upper limb. Clinically, the ULT frequencies are categorized into three distinct classes, including low-frequency (< 4.0 Hz), mid-frequency (4.0–7.0 Hz), and high-frequency (> 7.0 Hz) tremors. These ULT movements manifest as either oscillatory or rotational (angular displacement) motions, the so-called micro-Doppler effect (mDE). This study aims to develop a short-range (< 1.0 m) and contactless sensing method based on Doppler millimeter-wave (mm-Wave) radar for ULTs detection. The reflected electromagnetic waves indicate the time-varying frequency characteristics, which can be analyzed by using time-frequency transform (TFT) methods, such Wigner-Ville distribution (WVD) and smoothed pseudo WVD (SPWVD) methods. These TFT methods are used to extract the mDE features, which are subsequently visualized as color-coded spectrograms for ULTs classification. Then, a two- dimensional (2D) convolutional neural network (CNN) is employed to automatically recognize the visual feature patterns for ULTs classification based on frequency and amplitude information. In the experimental setup, the W-band (76–81 GHz) Doppler mm-Wave biosensor is implemented for sensing and extracting feature patterns. The proposed classifiers based on "WVD + 2D CNN" and "SPWVD + 2D CNN" are trained and validated by using the collected datasets, with 60% randomly selected for training datasets and 40% for testing datasets in each fold validation. The ten-fold cross-validation method is applied to evaluate the classifier's performances, achieving an average Precision of 95.92%, average Recall of 95.89%, average F1-score of 0.9509, and average Accuracy of 95.89%, respectively. The experimental results demonstrate the feasibility of the proposed classifier for real-time ULTs classification in PD patients using short-range (< 1.0 m) and contactless sensing.

Keywords: Parkinson's disease; upper limb tremor (ULT); micro-Doppler effect (mDE); point cloud map; short-range and contactless; time-frequency transform (TFT); convolutional neural network (CNN)

 doi:10.20944/preprints202604.2032.v1

1. Introduction

According to the Ministry of the Interior's (MOI) statistics in 2023 years, Taiwan's elderly population aged over 65 accounted for more than 20% of the total population, and the nation is expected to become a super-aged society (more than 25%) by 2025 [1,2]. In aging societies, neurodegenerative disorders are becoming increasingly prevalent among the elderly population, including Parkinson's disease (PD), Alzheimer's disease (AZD), dementia, and cerebellar atrophy. These diseases are characterized by a chronic progression, leading to a gradual decline in neurological function. Among these diseases, PD and AZD have the higher prevalence. In PD, the dopamine deficiency combined with impaired cholinergic function results in an inadequate supply of dopamine required for regulating muscle activity, leading to various motor dysfunctions [3]. In Europe, there are approximately 1.2 million PD patients, with an estimated 60,000 new cases diagnosed annually. In the United States, approximately 1.0

million people are affected by PD, and nearly 90,000 new cases are diagnosed with PD each year [4,5].

The onset of PD typically occurs between the ages of 40 and 60, and its incidence increases with age, significantly impacting the patient's quality of life. The PD is a neurodegenerative disorder that encompasses several types of movement disorders. Involuntary upper limb tremor (ULT) with different frequencies and amplitudes is one of the primary motor symptoms; and ULT frequencies are divided into three distinct classes: low-frequency (<4.0 Hz), mid-frequency (4.0–7.0 Hz), and high-frequency (>7.0 Hz) tremors. Parkinsonian tremor (PDT) and essential tremor (ET) are the primary tremor syndromes, encompassing various motor impairments and rhythmic oscillations that primarily affect either the left or right upper limb, including rest tremor (RT), postural tremor (PT), action tremor (AT), kinetic tremor (KT), physiological tremor, and pill-rolling tremor [6–11], and is sometimes accompanied by vocal modulation, affecting the vocal cords, respiratory muscles, and articulation, as well as mild gait abnormalities [12–15]. The PDT typically begins in one upper limb and may gradually extend to the head, lower limbs, trunk, and facial muscles. Clinically, PD is classified into five stages. In stages 1 to 3, patients with PD experience mild motor symptoms or develop walking and balance impairments, emphasizing the importance of early diagnosis and treatment. Selecting appropriate medications and rehabilitation strategies tailored to the specific type of neurodegenerative disease is crucial for effectively slowing its progression. Hence, the development of a digital-assisted quantification tool enables objective ULTs classification in patients with PD and facilitates self-care assessment.

Patients with PD usually exhibit some symptoms, such as ULTs, freezing of gait (FOG), bradykinesia, and dystonia [6–8,14–20]. Digital-assisted quantification tools have been utilized to detect FOGs and ULTs in the lower or upper limbs, respectively. The assistive tools for these two conditions include wearable sensors (accelerometers, gyroscopes, and pressure sensors), cameras or infrared sensors, millimeter- wave (mm-Wave) sensors [14–17], and IMU (inertial measurement unit) and EMG (electromyography) sensors [18,19,21]. The aforementioned assistive tools facilitate early detection, long-term continuous monitoring, and personalized rehabilitation for patients with PD. The measurement signals can be analyzed by using time-frequency transform (TFT) methods, such as short-time Fourier transform (STFT) and fast Fourier transform (FFT), to extract tremor intensity and frequency for further quantifying ULT levels to identify the PD severity [18,20,21]. Then, machine -learning (ML) or deep-learning (DL) based method can be used to design a classifier for recognizing feature pattern for ULTs classification, including support vector machine (SVM), recurrent neural network (RNN), visual geometry group (VGG, University of Oxford) CNN (convolutional neural network) with 16 or 19 layers, and residual network (ResNet) with 18 or 50 convolutional (Conv.) layers (ResNet-18 or ResNet-50) [7,10,11,19,22–25]. However, the aforementioned assistive tools rely on contact-based sensor patches on human body to measure the physiological signals, such as EMGs, EEGs (electroencephalogram), tremors, postures, and gaits [14–21,26,27]. These contact-based sensing methods need to collect large-scale measurement data for physiological signal analysis, statistical processing, and feature extraction, and integrate with classifiers for quantifying severity

 doi:10.20944/preprints202604.2032.v1

levels and classes. In addition, the contact-based sensing methods also require prolonged monitoring, which may lead to drawbacks such as discomfort, increased stress, restricted movement, and low participant acceptance [7,10,11,17,21,22].

Contactless sensing methods, such as hand-drawn Archimedean spirals [10,11,23,24] and mm-Wave sensor [7,28–30], offer non-wearable, short-range, and non- contact sensing with personalized and repeatable operations. The spiral trajectories of the drawn patterns can be digitized, and these drawn patterns highlight distinct differences between normal individuals and patients with PD. For feature analysis, time-domain parameters (such as zero crossing (ZC), waveform length (WL), and Willison amplitude (WAMP) [7]), polar coordinate features, and frequency-domain parameters [11,12,31,32] facilitate the identification of nonlinear patterns associated with different tremor classes. In addition, the STFT method can be used to extract the time- frequency feature parameters. By leveraging color- encoded feature patterns associated with varying ULT intensities, ML- and DL-based classifiers can also be trained for automated tremor classification, including low-frequency tremor, PDT, and ET symptoms. However, the hand-drawing method must be correlated with the MDS-UPDRS (Movement Disorder Society's Unified Parkinson's Disease Rating Scale) assessment (0 to 4 scoring levels) [33,34] to define the severity levels and ULT classes. Thus, digital assistive tools, such as an iPad with Apple Pencil or ink pen or a touch screen [11,12,31,32], remain essential for efficient data collection and analysis. Additionally, the evaluation process is significantly time-consuming.

The mm-Wave sensors (as seen in Figure 1), such as X-band (8-20 GHz), V-band (57-64 GHz), or W-band (76-81GHz) frequencies, enable short-range and contactless detection for identifying and tracking the dynamic objects, including ULT, respiration, heartbeats, and body gesture monitoring [7,35–39]. Low-frequency X-band sensor is suit for longer range detection and better penetration through obstacles for big object movements, but has lower resolution for detecting small and fine movements. The mid-frequency V-band sensor offers higher resolution for small and fine movement detection, but suffers from high atmospheric absorption, resulting in suit for short-range sensing. The high- frequency W-band sensor also provides the best resolution for precise motion tracking for small and fine movements in short-range sensing. The ULT movements can manifest as either regular or irregular oscillations with symmetrical or asymmetrical amplitudes, sometimes accompanied by subtle rotational motions, the so-called micro-Doppler effect (mDE). Hence, we select the W-band Doppler mm-Wave radar [38,39] to establish a short-range and contactless biosensor for detecting subtle upper limb displacements which relies on reflected electromagnetic signal to analyze the object's motions without physical contact. The object's motions will result in reflected electromagnetic signals with time-varying velocity variations and frequency shifts, which can be represented as a point cloud map. Then, the TFT methods, such as Wigner-Ville distribution (WVD) and smoothed pseudo WVD (SPWVD) methods [40–42], are employed to extract the power spectrum from the time-domain micro-Doppler signatures (mDSs) and to generate the 2D (two-dimensional) colored visualization feature patterns, as seen in Figure 1. The aforementioned WVD provide promising time-frequency resolution for analyzing nonlinear and time-varying frequency signals, while also preserves the total signal energy to represent the power distribution across both time and frequency domains. The SPWVD method applies a smoothing kernel window to the WVD process, effectively reducing cross-term interference while maintaining high-resolution features. Both WVD and SPWVD can handle the time–frequency varying signals, making them suitable for real-time mm-Wave sensing applications, and also significantly enhances the structural clarity of the tremor feature representations, thereby improving the discriminability of different ULT classes. Thus, the resulting feature patterns are fed into a one-dimensional (1D) and 2D convolutional neural networks (CNNs) based classifiers to automatically perform the ULT identification and possible disease classification across various tremor frequency ranges, enhancing the differentiation of tremor patterns and their underlying causes, as seen in Figure 1.

 doi:10.20944/preprints202604.2032.v1

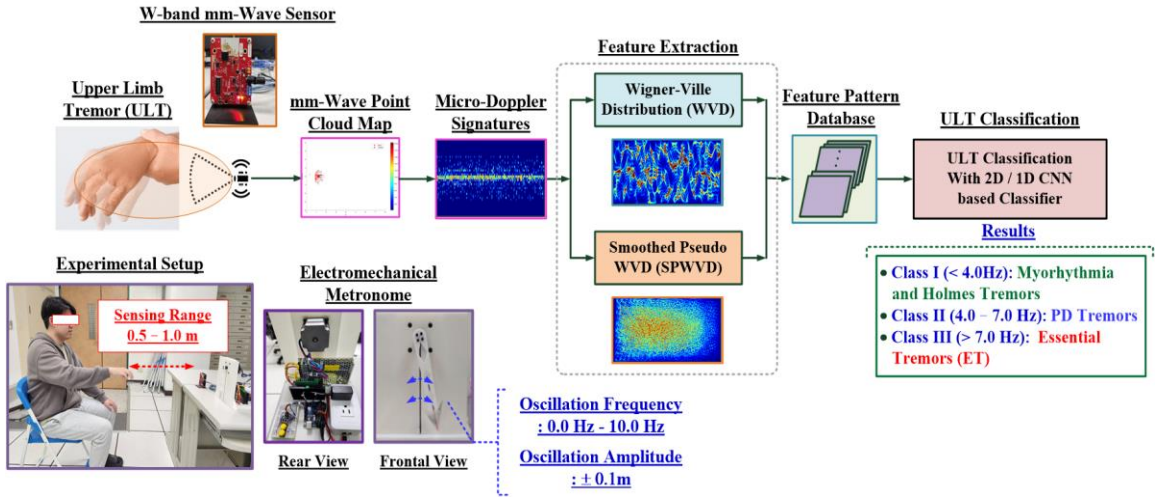

Figure 1. Configuration of W-band mm-Wave based biosensor and experimental setup for ULT detection and Classification.

The experimental setup was conducted in a laboratory environment (as seen in Figure 1), and the short-range and contactless sensing framework was established by W-band mm-Wave based biosensor (Texas Instruments (TI), Dallas, USA). The proposed mm-Wave biosensor was placed on the desk in front of the enrolled subject with sensing range, 0.5-1.0 m, to sense the ULTs. An electromechanical metronome was employed to generate the driving force by using a pulse-width modulation (PWM) controller [7], and operated within an oscillation frequency range of 0.0 Hz to 10.0 Hz. Referring to the metronome, each enrolled subject was instructed to simulated ULT movements with rhythmic and symmetrical or asymmetrical oscillations at each sensing range, maintaining an oscillation amplitude of ± 0.1 m. The oscillation frequencies were divided into three classes: Class I (< 4.0 Hz), Class II (4.0-7.0 Hz), and Class III (> 7.0 Hz). The raw mDSs of different ULTs were collected and processed for feature extraction with the WVD and SPWVD methods. Hence, the color- encoded feature patterns could be collected and be divided into training and testing datasets for trained and validated the proposed classifier models, including "WVD + 1D CNN or 2D CNN classifier" and "SPWVD + 1D CNN or 2D CNN classifier". A ten-fold cross validation method was adopted, in which 60% of the dataset was randomly selected for training datasets and the remaining 40% was used as the testing datasets in each fold. The classifier's performances were evaluated using Precision(%), Recall (%), F1 Score, and Accuracy(%). The experimental results demonstrated the feasibility of the proposed classifier model and the most suitable sensing range for real-time ULT classification.

2. Methodology and Materials

2.1. Principles of Contactless W-Band (76- 81 GHz) mm-Wave Based Biosensor

As seen the experimental setup in Figure 1, the W-band mm-Wave firmware used is a 76-81 GHz mm-Wave based Doppler radar with 2 Txs (2-transmit) and 4 Rxs (4-receive) phased array antennas, offering a 120° azimuth field of view (FoV) and a 30° elevation FoV and a substantial 4 GHz of continuous bandwidth (BW); and Rx noise figure is 14 dB for the 76-77 GHz and 15 dB for the 77-81 GHz. This HW-SW (hardware–software) device is an integrated single-chip mm-Wave sensor (ARM® Cortex®-R4F-based radio control system) based on frequency modulated continuous-wave (FMCW) radar platform, consisting of an mm-Wave sensor (IWR1642 BOOST# Evaluation Module) and Python application software. The proposed mm-Wave biosensor transmits electromagnetic waves via 2 Txs towards dynamic objects, which reflect the electromagnetic waves back to 4 Rxs, as seen the configuration in Figure 2. After capturing and preprocessing the reflected electromagnetic signals, the displacement (amplitude) and velocity (frequency) changes caused by the objects can be detected,

 doi:10.20944/preprints202604.2032.v1

allowing for estimating the object's movement state, distance, velocity, direction, or angle. Assuming the transmitted electromagnetic signal is $s(t)$ [7]

$$s(t) = A_0 \cos(2\pi f_0 t) \quad (01)$$

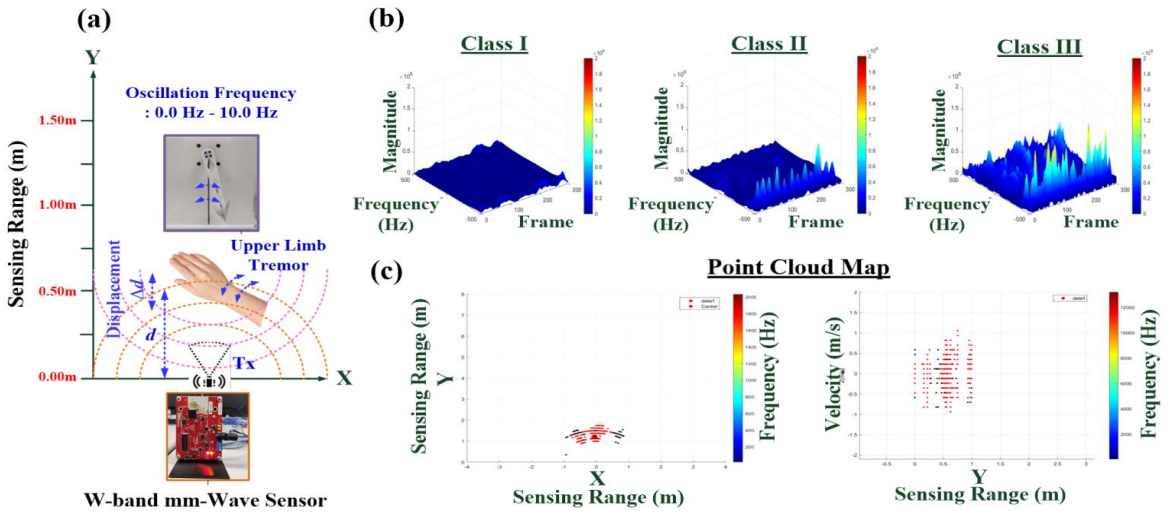

Figure 2. Short-range sensing experimental setup, mm-Wave signal processing, and feature parameters extraction. (a) Distance estimation between.

Tx and desired object, (b) Range- and Doppler-FFT processing for three classeses, (c) Feature parameters extraction (X, Y, Z(m/sec))

where A_0 is the signal amplitude; f_0 is the signal frequency. Given f_T and $\theta(t)$ as the transmitted frequency and phase noise, respectively, the reflected electromagnetic signal, $R(t)$, can be represented as [7]

$$\mathrm{R}(t) \approx A_{\mathrm{R}} \cos(2\pi f_{\mathrm{T}} t) - \frac{4\pi d_0}{\lambda_T} - \frac{4\pi x(t)}{\lambda_T} + \theta(t - \frac{2d_0}{c})) \quad (02)$$

$$x(t) = A_1 \cos(2\pi f_1 t) \quad (03)$$

where A_R is the amplitude of the reflected signal, $R(t)$; $\lambda_T = c/f_T$ is the wavelength ($c = 3 \times 10^8$ m/s); and $d_0 = ct_r/2$ is the distance between the object and the Txs, t_r is a delay time on the time axis. For ULT detection, $x(t)$ is the ULT's dynamic movement signal, f_1 is the tremor oscillation frequency (irregular or regular) and A_1 is the tremor oscillation amplitude (symmetrical or asymmetrical). Assuming $\theta_0 = 4\pi d_0/\lambda_T$ as the phase shift and $\Delta\theta(t) = \theta(t) - \theta(t\text{-}2d_0/c)$ as the residual phase noise, the normalized baseband signal, $B(t)$, can be obtained through the mixing and low-pass filtering processes, and then an intermediate frequency (IF) signal is generated, which contains crucial information, including object's angle., distance, and velocity [7]

$$B(t) \approx \cos(\theta_0 + \frac{4\pi x(t)}{\lambda_T} + \Delta\theta(t)) \quad (04)$$

Considering phase angle, θ_0, as an odd multiple of $\pi/2$, and $s(t) \ll \lambda_T$, Equation (04) can be simplified to the general mathematical form as Equation (05):

$$B(t) \approx \frac{4\pi x(t)}{\lambda_T} + \Delta\theta(t), \quad x(t) \approx d_0 \pm \Delta d(t) \quad (05)$$

where $\Delta d(t)$ is the object's variation range with regular or irregular motions. If phased array antennas are used, the synthesized signal for multi channels is

$$x_T(t) = \sum_{i=1}^{T} B_i(t), \; i = 1, 2, \ldots, T \; (T = 4 \text{ in this study}) \quad (06)$$

The synthesized signal, $x_T(t)$, can be processed through an analog-to-digital converter (ADC), which then sends the digital raw data to an embedded system or a laptop. After digital filtering

 doi:10.20944/preprints202604.2032.v1

removes unwanted high-frequency and low- frequency components, the objects' displacement and velocity changes are estimated through Range-FFT and Doppler-FFT processes.

Before digital mm-Wave signal processing, the sensing data stream can be stored in an $N \times M$ matrix, where M represents the number of chirps and N represents the number of samples per chirp signal. In mm-Wave signal processing, each chirp signal is sequentially read and processed through the Range-FFT and Doppler-FFT processes, target searching, phase extraction, phase unwrapping, phase difference operation, and filtering processes, as seen in Figure 2. The two key signal processing, Range-FFT and Doppler-FFT operations, are used to estimate the range, displacement, and velocity changes of the detected potential objects. The tw operations are described as follows:

- Range-FFT processing: the synthesized IF signal, $x_T(t)$, is processed using a 1D FFT to extract the distance information between the desired object and the Tx; and then produces a time delay τ (sec) between them and results in a frequency tone, S_τ By performing Range- FFT operation, the frequency response of the chirp signal (the signal $x_T(t)$ in Equation (06)) can be estimated for finding out the peak value of the frequency spectrum (as seen Range- and Doppler-FFT processing for three classes in Figure 2(b)). Then, the distance (location), d, between the desired object and the Tx can be determined (as seen distance estimation in Figure 2(a)) by general form as

$$d = \frac{cT_c}{2B} S_\tau(m), \quad S = \frac{B}{T_c}, \quad S_\tau = S\tau \quad (07)$$

where $c = 3 \times 10^8$ (m/s) is the velocity of electromagnetic waves in the air; B is the bandwidth; T_c is the timing duration; and S is the slope of the chirp signal.

- Doppler-FFT process: capturing M chirps results in M phases, and treating these M phases as a signal and performing an FFT operation, the velocity of desired object can be estimated by using the peak values obtained from every two phases as follows:

$$v = \frac{\lambda \Delta\theta}{4\pi T_c} \text{ (m/sec)}, \quad v = \frac{\lambda \Delta\theta}{4\pi T_c}, \quad \Delta\theta < \pi \quad (08)$$

where phase differences, $\Delta\theta$, can be obtained through the Direction of Arrival Estimation (DoAE) and Angle Estimation (as seen the flowchart in Figure 3); and λ is the wavelength of electromagnetic wave. Hence, the 1D Range-FFT operation can be used to estimate the distance of the possible desired object; thus, the objects' dynamical displacement information can be obtained. The 2D Doppler-FFT operation can detect the velocity of the desired object motions. As seen the flowchart in Figure 3, this study employs the 1D Range-FFT operation to estimate the displacement variations caused by symmetrical or asymmetrical ULTs; after the Range-FFT processing, the 2D Doppler-FFT is applied to the consecutive frames (chirp sequences) along the time axis to obtain the object's moving velocity information, as seen the point cloud map (X, Y, Z(m/sec)) in Figure 2(c).

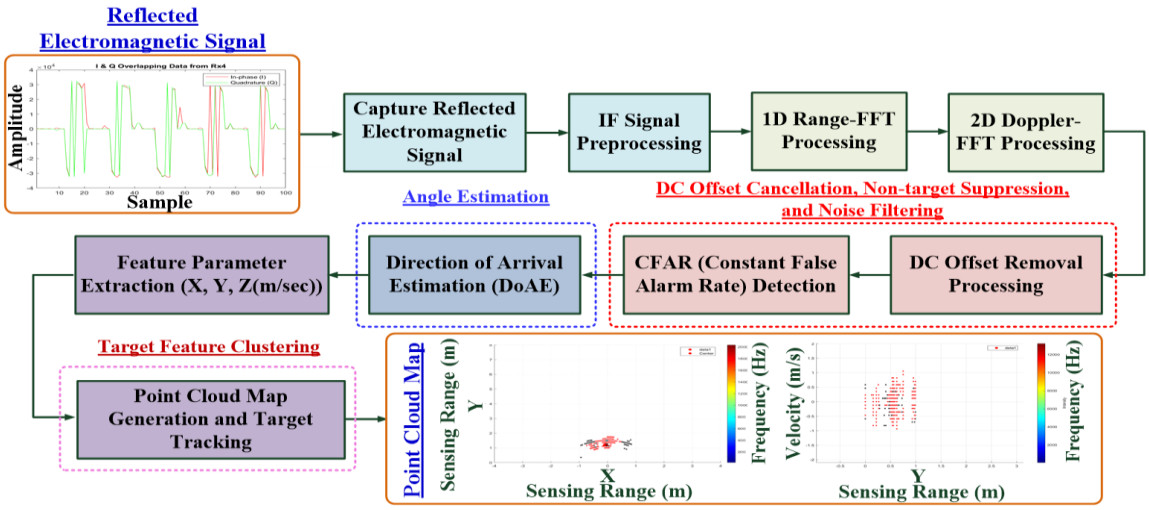

Figure 3. Flowchart of mm-Wave signal processing and feature parameters extraction (Point Cloud Map Generation).

 doi:10.20944/preprints202604.2032.v1

2.2. Micro-Doppler Feature Extraction and Enhancement

The ULT refers to irregular or regular oscillatory motion and is characterized by symmetrical or asymmetrical amplitudes, as well as rotational or vibratory components in upper limb movements. These subtle motions cause small but distinguishable frequency shifts superimposed on the reflected signals, resulting in unique micro-Doppler (mD) feature patterns. With the 300-frame (33.33ms per frame) data acquisition window lengths for framing processes, the mD feature patterns can be extracted from point cloud map, as seen the feature patterns for three ULT classes in Table 1, which can be used to distinguish the mD feature patterns among three ULT classes related to different tremor frequency, oscillation and or rotational motions. For the time-frequency analysis, the WVD and SPWVD based TFT methods can enhance the resolutions of mD feature pattern for refined color visual representations and then generate the 2D color-encoded feature patterns, as seen the 875 × 656 pixels patterns in Table 1. Theses TFT methods are used to analyze the variations of mD feature patterns in both time and frequency domains. Comparison with STFT method, the WVD method provides higher time-frequency resolution by applying the Fourier transform to the time-dependent autocorrelation function, $R(t,\tau)$, and the power spectrum is transformed into a time-dependent function, "$R(t,\tau)\bullet \exp(-j2\pi f\tau)$", allowing to extract the frequency parameters of the signal $x_T(t)$ within a specific time range, including instantaneous frequency, frequency centroid, and energy distribution. The extracted feature patterns can be transformed into a color-encoded representation as shown in Table 1. The general formula of WVD for signal $x_T(t)$ is defined as [40–42]:

$$WVD(t,f)=\int_{-\infty}^{+\infty} z(t+\frac{\tau}{2})z^*(t-\frac{\tau}{2})e^{-j2\pi f\tau}d\tau\,,\quad R(t,\tau)=z(t+\frac{\tau}{2})z^*(t-\frac{\tau}{2}) \quad (09)$$

$$z(t)=x_T(t)+jH[x_T(t)] \quad (10)$$

where τ *is* the timing shift; $\omega=2\pi f$ and f *a*is frequency; $z^*(\bullet)$ is the complex conjugate operation; and $H[\bullet]$ is the Hilbert transform operation for signal $x_T(t)$. The Fourier transform of the time-dependent autocorrelation function can by computed by integral operation. However, while signal contains multiple frequency components, the WVD has cross-term interferences, leading to spectral interferences, readability decreasing, and negative energy artifacts in the spectrogram, and will affect the clarity of time-frequency feature patterns. Hence, the SPWVD method can reduce aforementioned interferences through time and frequency smoothing processes. The general formula is defined as [40–42]:

$$SPWVD(t,f)=\int_{-\infty}^{+\infty}\int_{-\infty}^{+\infty} g(\tau)h(f)x_T(t+\frac{\tau}{2})x_T^*(t-\frac{\tau}{2})e^{-j2\pi f\tau}d\tau df \quad (11)$$

where $g(\tau)$ is the smoothing window along the time-axis; and $h(f)$is the smoothing window in the frequency direction. In this study, "Hamming window" is chosen as both the time and frequency domain windows, which are used to reduce time-domain interference and to suppress cross-terms in the frequency domain. Hence, it can reduce the cross-term interferences while also maintaining the time-frequency features and enhancing resolution, thereby improving the distinguishability among different ULT classes.

For feature extraction, this study employs the WVD and SPWVD based TFT methods to extract feature patterns of different ULT motions as pathological oscillation frequencies in three ranges: Class I: < 4.0 Hz; Class II: 4.0-7.0 Hz; and Class III: > 7.0 Hz, along with their corresponding possible ULT classes, including Myorhythmia and Holmes tremors, PDT (RT and PT), and ET (PT and KT) [7,30], as seen in Table 1. Experimental setup was conducted in our university laboratory (Micro- processor Laboratory, National Chin-Yi University of Technology (NCYUT), Taichung City, as seen in Figure 1), and each enrolled subject was asked to sit on a chair in front of a desk. Referring to the metronome with varying oscillation frequencies from 0.0 Hz to 10.0 Hz, each enrolled subject simulated ULT motions at different measurement sites from 0.50 m to 1.50 m (as seen in Figure 2(a)). For two repeated measurements at each visiting site, we could collect raw datasets of resting condition and three ULT classes. For each visiting site, two repeated measurements were conducted to collect raw datasets under resting conditions and across three ULT classes. The feature patterns were extracted from collected raw datasets by using WVD and SPWVD methods, which could be divided into training

 doi:10.20944/preprints202604.2032.v1

datasets and testing datasets, as seen in Table 2. Subsequently, these datasets were used to train and validate the "WVD + 2D CNN", "WVD + 1D CNN", "SPWVD + 2D CNN", and "SPWVD + 1D CNN" based classifiers, as seen the structures in Figure 4.

Table 1. Feature extraction and enhancement with WVD and SPWVD processes for three ULT classes.

ULT Class [7,30]	mD Feature Pattern	WVD Processing	SPWVD Processing
Resting Condition Normal	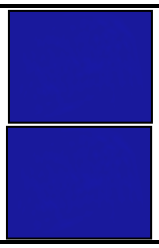	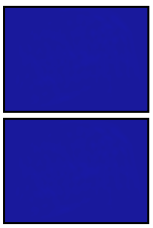	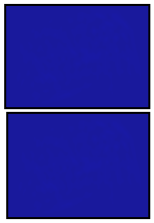
Class I: < 4.0 Hz Low Frequency: Myorhythmia and Holmes Tremors	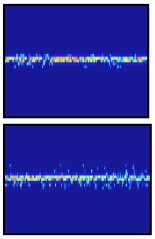	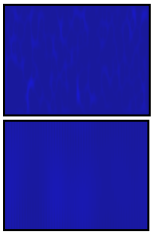	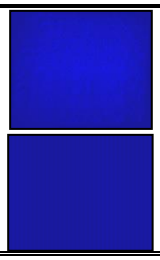
Class II: 4.0-7.0 Hz Medium Frequency: Parkinsonian Tremor (PDT) RT (4-6 Hz), PT (6-8 Hz)	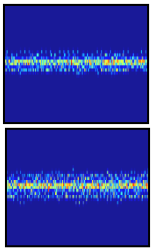	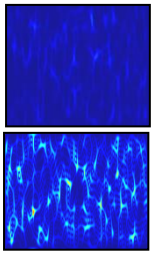	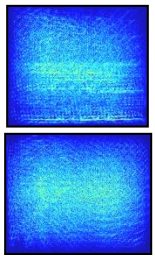
Class III: > 7.0 Hz High Frequency: Essential Tremor (ET) PT (5-8 Hz), KT (5-12 Hz)	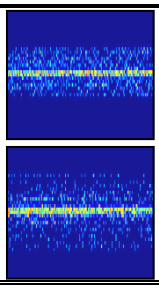	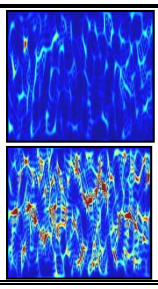	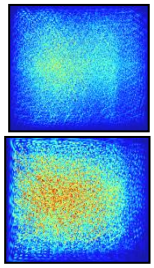

Table 2. Datasets at different measurement sites from 0.50 m to 1.50 m for three ULT classes.

Measurement Site (m)		0.50	1.00	1.50	Feature Extraction Method
Training Dataset	Class I	170	170	170	micro-Doppler (mD) Features +WVD
	Class II	190	190	190	
	Class III	140	140	140	
Testing Dataset	Class I	170	170	170	micro-Doppler (mD) Features + SPWVD
	Class II	190	190	190	
	Class III	140	140	140	
Total		1,000	1,000	1,000	

Preprints.org (www.preprints.org) | NOT PEER-REVIEWED | Posted: 29 April 2026 doi:10.20944/preprints202604.2032.v1

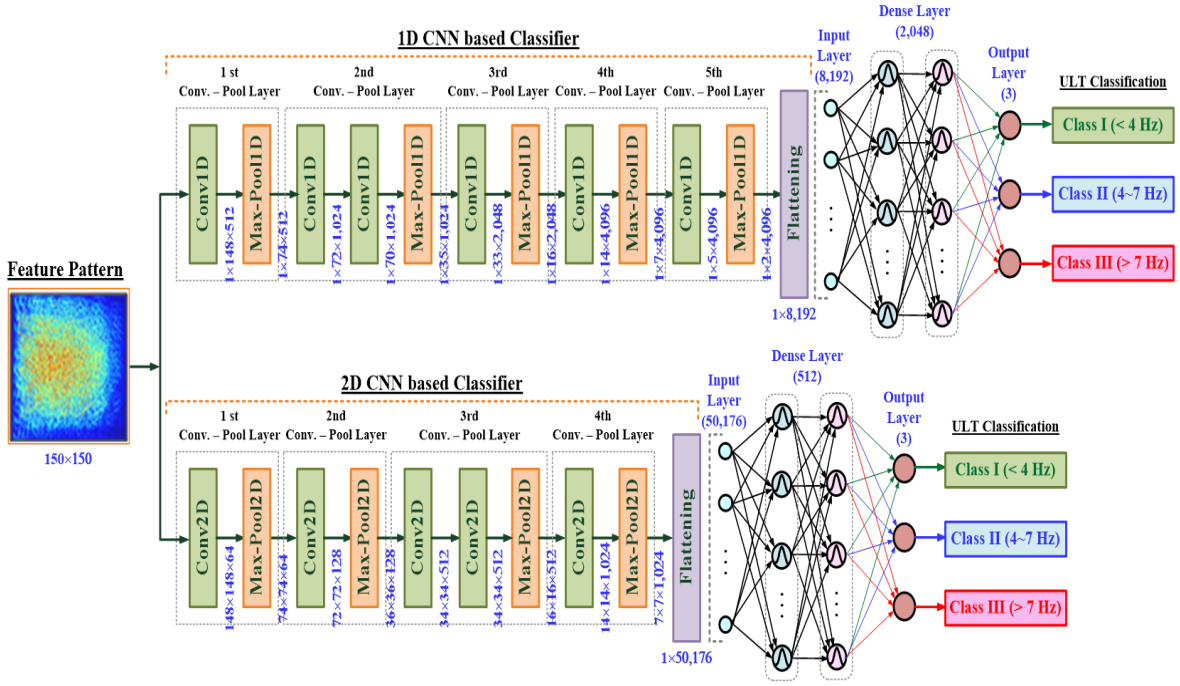

Figure 4. Structure of the proposed 1D CNN and 2D CNN based classifiers for ULT classification.

2.3. Pattern Classifier Design

The small-scale model of cascade CNN (CCNN) was used to establish the 2D CNN and 1D CNN based classifiers, respectively, including "WVD+2D CNN", "WVD+1D CNN", "SPWVD+2D CNN", and "SPWVD+1D CNN". The aforementioned classifiers can perform the pattern recognition tasks for ULTs classification. The optimal classifier model, feature representations, and measurement sites are also evaluated, along with the applicability of the proposed DL-based model for the intended application. These CCNNs consist of multi convolutional–pooling (Conv.–Pool) layers, one flattening layer, and a fully connected layer (classification layer) with multi dense networks [22–24,39], which can be trained to automatically enhance features, extract features, and perform the pattern recognition tasks. Through multi Conv. operations with multi sliding 3×3 kernel windows, the multi Conv.- Pool layers can obtain a weighted linear combination of convolution kernels to raise both the depth and width levels of feature patterns. The multi Conv. operations can also increase the dimensionality, non-linearity, and complexity of feature patterns, thereby enhancing the classifier's ability to recognize complex feature patterns. By applying the maximum pooling (Max-Pool) operations, these processes can reduce the size of the feature patterns and can also maintain the key feature parameters while preserving the depth level of the feature patterns. The 4 2D Conv.–Pool layers and 5 1D Conv.—Pool layers are designed for 2D and 1D CNN based classifiers, respectively, as seen in Figure 4. Hence, the CCNN can directly extract features from 2D color-encoded feature patterns, and resize the input pattern size from 875×656 pixels to 150×150 pixels for training and validating the classifiers. The fully connected layer consists of a flattening layer, multi dense networks, and an output layer. In each dense network, every neuron node is connected to all neuron nodes in the preceding and succeeding layers, allowing it to receive inputs from all neuron nodes in the previous layer. The output y of each neuron node can be computed by the general formula [39,43,44]

$$y(W, x) = f(Wx + b) \quad (12)$$

where x is the input feature vector; W is weighted matrix in each dense network; b is the bias weight; and function $f(\bullet)$ is the activation function, and the GeLU (Gaussian error linear unit) function is used instead of traditional ReLU (rectified linear unit) function, which can mitigate the problem of gradient vanishing [39,44,45]. The dense networks are descending powers base on the number of input data

 doi:10.20944/preprints202604.2032.v1

and output classes (3 Classes), and their relevant design parameters for 2D CNN and 1D CNN based classifiers are depicted in Figure 4.

For multi-class classification problems, the categorical cross-entropy (CCE) based loss function (LF) is employed to evaluate the performance of classifier training, which measures the dissimilarity between the target labels and the predicted probability distribution output by a classifier. The CCE general formula is defined as [39,43,44]

$$LF = \sum_{k=1}^{K} \sum_{j=1}^{C} y_{k,j} \log(y'_{k,j}) \quad (13)$$

where $y_{k,j}$ is the target label with the "one-hot encoded" as [1, 0, 0], [0, 1, 0], and [0, 0, 1] for three classes, respectively; $y'_{k,j}$ is the predicted probability of jth class ($C = 3$) for kth training dataset (k = 1, 2, 3, …, K). The logarithm operation, log(•), can ensure that incorrect predictions are penalized more severely. The Softmax activation function is used in final output layer for multi classes, the Softmax general formula is defined as [44,45]

$$y'_j = \frac{\exp(z_j)}{\sum_{j=1}^{3} \exp(z_j)}, j = 1, 2, 3 \quad (14)$$

where z_j are the raw logits for jth class, as output vector $Z = [z_1, z_2, z_3]$; and exp(z_j) operator exponentiates the logits to make them positive value. The higher logits lead to higher probabilities, and the highest probability class is the possible classifier's prediction. The optimization algorithm, such as adaptive moment estimation (ADAM) optimizer, is employed to train the 2D CNN and 1D CNN classifier models to minimize the CCE LF. It utilizes iterative computations with smoothing and adaptive updates, and an adjustable learning rate to enhance training efficiency. The mean and variance of gradients with bias-corrected estimates are used to update the classifier's parameters for mitigating the vanishing and exploding gradient problems. Finally, the ten-fold cross- validation method is applied to evaluate the classifier's performance. The feasibility of the proposed classifier is assessed by using Precision (%), Recall (%), F1 Score, and Accuracy (%) as evaluation metrics [39,43].

3. Experimental Results and Discussion

3.1. Case Study 1: Classifier Training and Validation in a Fixed Measurement Site

Experiments were conducted in a university laboratory environment, as seen Micro-processor Laboratory in Figure 1. Ten enrolled subjects (Gender: male subject, Age: 22.5 ± 2.5 years old) were invited, and each enrolled subject was asked to sit on a chair in front of a desk with each participant undergoing two test sessions. The W-band mm-Wave based biosensor was placed at different measurement sites, as sensing ranges from 0.50 m to 1.50 m, as seen in Figure 2(a). Measurements were taken with data acquisition lengths of 300 sequential frames (each experiment lasted approximately 10 sec) at three different locations (0.50 m, 1.00m, and 1.50 m). Referring to the metronome with varying 0.0 Hz to 10.0 Hz oscillation frequencies, each enrolled subject simulated regular or irregular ULT motion with symmetrical or asymmetrical amplitudes in three ranges of oscillation frequencies: (1) < 4.0 Hz, (2) 4.0-7.0 Hz, and (3) > 7.0 Hz. The numbers of collected raw measurement data at different measurement sites for three classes were presented in Table 2. A total of 1,000 raw datasets were collected and could be divided into 500 for training datasets and 500 for testing datasets at each measurement sites, respectively. The "mD feature pattern + WVD" and "mD feature pattern + SPWVD" were used to extract the colored visualization feature patterns (as shown in Table 1) for trained 2D and 1D CNN based classifiers. This study designed CCNN architectures to realize pattern- recognition classifiers, as seen in Figure 4. Different CCNN architectures were implemented in a computer based platform (Intel® Q370, Intel® Core™ i7 8700, DDR4 2400MHz 8G*3) and also used the graphics processing unit (GPU: NVIDIA® GeForce® RTX™ 2080 Ti, 1755MHz, 11GB GDDR6) [50] to speed up the execution time for ULTs classification. For example, in Figure 4, as 2D CNN, first two Conv.-Pool layers were used to extract the initial feature parameters and then second

 doi:10.20944/preprints202604.2032.v1

two Conv.—Pool layers were employed to refine the extracted features and removes redundant information (from $148 \times 148 \times 64$ to $7 \times 7 \times 1{,}024$). The dense network ($50{,}176 \times 512 \times 3$) performed the classification tasks based on high-level refined feature patterns.

The ADAM optimizer's learning rate, momentum decay, and variance decay were set as 0.001, 0.900, and 0.999 (experience values) [39,43] and the maximum number of training iterations was set as 150 epochs. An iteration computational manner was employed to adjust the network parameters. For each ULT Class of datasets, 60% of training datasets were randomly used for classifier training, distributed as follows: Class I: 102, Class II: 114, and Class III: 84, and the remaining 40% for classifier testing, distributed as follows: Class I: 68, Class II: 76, and Class III: 56, respectively. Then, the ADAM optimizer was used to train the 2D and 1D CNN-based classifiers with 300 training datasets. The 200 testing datasets were utilized to evaluate the classifier's recognition performance. We conducted case study to train and validate the proposed classifiers in a fixed 0.50 m measurement site. This experimental setup ensured consistency in data acquisition, enabling a reliable evaluation for the classifier's performances. For example, "SPWVD + 2D CNN" based classifier, Figures 5(a) and 5(b) showed the training (train: blue line) and validation (val: orange line) history curves for accuracy saturation curves and convergence history curves, respectively. As increased the iteration numbers, the classifier's output accuracy smoothly increased; conversely, the LF value gradually decreased to the specific convergence condition, and the val_loss followed train_loss without large divergence, which reached saturation state after 60 training epochs. Hence, with the 10-fold cross validation, an average Accuracy (%) of $95.89 \pm 0.62\%$ and an average loss value of 0.1244 ± 0.0012 were obtained after approximately 60 epochs. As seen testing results in Table 3, for the fixed 0.50 m measurement site, the 10-fold cross validation results demonstrated that the performance of "SPWVD + 2D CNN" was better than the other 3 classifier models ("WVD + 2D CNN", "WVD + 1D CNN", and "SPWVD + 1D CNN"), as the average F1 score was greater than 0.9000 (approaching to 1, indicated a promising classifier that effectively balanced precision and recall), and average Accuracy (%) was also higher than other 2D and 1D CNN models. Hence, Case Study#1 suggested the following: (1) the promising classifier model could be determined by combing SPWVD based feature extractor and 2D CNN, as seen the grey highlights in Table 3; (2) 2D CNN was effective for 2D spatial patterns, such as time-frequency spectrograms; and (3) 2D Conv. operations increased the dimensionality and non-linearity of feature patterns to enhance the ability to recognize the complexity feature patterns.

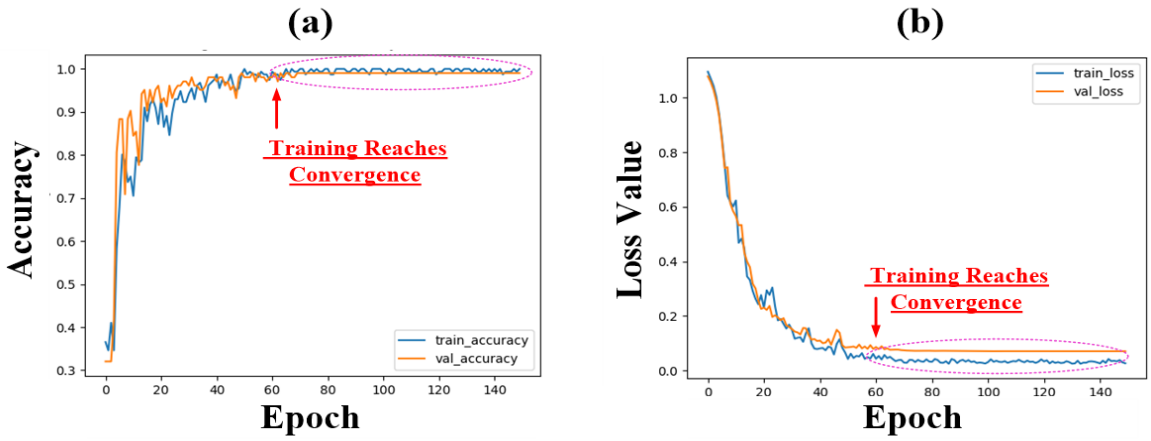

Figure 5. Training and validation history curves (train: blue line, val: orange line). (a) History curve of Accuracy versus Epoch, (b) History curve of Loss value versus Epoch.

Table 3. Testing results of 10-fold cross validation for "WVD + 2D CNN", "SPWVD + 2D CNN", "WVD + 1D CNN", and "SPWVD + 1D CNN" based classifiers at the fixed 0.50 m measurement site.

 doi:10.20944/preprints202604.2032.v1

Method	Average Loss Value	Average Precision(%)	Average Recall(%)	Average F1 Score	Average Accuracy(%)
WVD + 2D CNN	0.2309 ± 0.0020	93.86 ± 1.89	93.81 ± 1.88	0.9379 ± 0.1900	93.81 ± 1.88
SPWVD + 2D CNN	0.1244 ± 0.0012	95.92 ± 0.60	95.89 ± 0.62	0.9588 ± 0.0060	95.89 ± 0.62
WVD + 1D CNN	0.2798 ± 0.0020	90.35 ± 1.95	90.22 ± 2.01	0.9014 ± 0.0020	90.22 ± 2.01
SPWVD + 1D CNN	0.2942 ± 0.0020	88.25 ± 1.39	88.21 ± 1.37	0.8816 ± 0.0130	88.21 ± 1.37

3.2. Case Study 2: Classifier Validation in Different Measurement Sites

To validate the feasibility of short-range continuous monitoring, we asked each enrolled subject to place the right or left upper limb at three locations, 0.50 m, 1.00 m, and 1.50 m under resting condition, as seen in Figure 2(a). For the same experimental setup, referring to the metronome, each enrolled subject was instructed to maintain a stationary upper limb and to simulate ULTs with symmetrical ± 0.1 m oscillation amplitudes and different pathological frequencies at different measurement sites, including Class I: < 4.0 Hz, Class II: 4.0-7.0 Hz, and Class III: > 7.0 Hz. The raw sensing ULT signals could also be collected for signal preprocessing and feature extraction with WVD and SPWVD. In an additional 2,000 experimental tests at locations 1.00 and 1.50 m (as seen Table 2), the training and testing datasets were also prepared for trained four classifier models, as seen in Table 4. We also evaluated the different classifiers' performances at different measurement sites by using the F1 score (the harmonic mean of precision and recall) and Accuracy (%) indexes. With the 10-fold cross validation, the average F1 score and average Accuracy(%) at different sensing ranges for four classifier models were shown in Table 4, respectively. The key feature parameters gradually diminished as the sensing range increased from 0.50 m to 1.50 m, due to the attenuation of the radar microwave signal intensity. Therefore, the attenuated feature patterns would affect the classifier's pattern recognition capability. Two key evaluation indexes decreased as the sensing ranges increased for the aforementioned four classifiers. It could be seen that the promising measurement site at "*location 0.50 m*" for ULTs monitoring and classification with "SPWVD + 2D CNN" and "WVD + 2D CNN" based classifiers. The average F1 scores for both classifiers were 0.9588 ± 0.0060 and were greater than 0.9000, meaning that classifier had few false positives and false negatives and underscoring the classifiers' reliability in differentiating the three tremor classes. The average Accuracy (%) was 95.89 ± 0.62% for identified the tremor classes. Overall testing results for four classifier models were shown in Table 4.

For the same datasets and measurement site at location 0.50 m, with the 10-fold cross validation, "SPWVD + 1D CNN " had average Precision (%) of 88.25 ± 1.39%, average Recall (%) of 88.21 ± 1.37%, average of F1 score of 0.8816 ± 0.0130, and average Accuracy (%) of 88.21 ± 1.37% for ULTs classification, and the experimental results of "WVD + 1D CNN" was better than aforementioned 1D CNN model [46,47]. For overall experimental results, it could be seen the 2D CNN models outperformed the 1D CNN models across different measurement sites. Hence, Case Study#2 suggested the following: (1) the promising measurement site could be set at location 0.5 m, and desktop sensing tool was feasibility for a short-range and contactless continuous monitoring; (2) feature extraction from time-frequency spectrogram based on 2D spatial dimensions was beneficial for pattern recognition; (3) multi Conv.–Pool operations with multi Conv. kernel windows were used to establish a CCNN for progressively captured both fine and coarse features to improve accuracy in pattern recognition tasks; (4) multi Conv. layers in a sequential manner could filter out irrelevant

 doi:10.20944/preprints202604.2032.v1

information, enabling a progressive learning approach that improved robustness to variations in input feature patterns.

Table 4. Testing results of 10-fold cross validation for different classifier models and measurement sites.

Method	Site(m)	Average Loss Value	Average Precision(%)	Average Recall(%)	Average F1 Score	Average Accuracy(%)
WVD + 2D CNN	0.50	0.2309 ± 0.0020	93.86 ± 1.89	93.81 ± 1.88	0.9379 ± 0.1900	93.81 ± 1.88
	1.00	0.3126 ± 0.0030	88.25 ± 1.32	88.22 ± 1.30	0.8817 ± 0.1300	88.22 ± 1.30
	1.50	0.3903 ± 0.0030	85.42 ± 4.93	85.41 ± 4.67	0.8509 ± 0.0480	85.41 ± 4.67
SPWVD + 2D CNN	0.50	0.1244 ± 0.0012	95.92 ± 0.60	95.89 ± 0.62	0.9588 ± 0.0060	95.89 ± 0.62
	1.00	0.3816 ± 0.0030	87.39 ± 2.06	86.90 ± 1.93	0.8684 ± 0.1960	86.90 ± 1.93
	1.50	0.3357 ± 0.0030	85.98 ± 2.58	85.57 ± 2.27	0.8546 ± 0.0230	85.57 ± 2.27
WVD + 1D CNN	0.50	0.2798 ± 0.0020	90.35 ± 1.95	90.22 ± 2.01	0.9014 ± 0.0020	90.22 ± 2.01
	1.00	0.3855 ± 0.0030	83.57 ± 2.06	83.60 ± 2.06	0.8331 ± 0.0210	83.60 ± 2.06
	1.50	0.5077 ± 0.0040	79.87 ± 5.94	79.66 ± 5.93	0.7922 ± 0.0640	79.66 ± 5.93
SPWVD + 1D CNN	0.50	0.2942 ± 0.0020	88.25 ± 1.39	88.21 ± 1.37	0.8816 ± 0.0130	88.21 ± 1.37
	1.00	0.4439 ± 0.0040	80.66 ± 1.73	83.57 ± 1.12	0.8150 ± 0.1530	83.57 ± 1.12
	1.50	0.3216 ± 0.0030	81.51 ± 3.63	81.49 ± 3.51	0.8127 ± 0.0350	81.49 ± 3.51

3.3. Comparison with Existing Non-Contact and Short Range Sensing Methods

Table 5 indicated the existing short-range and non- contact sensing methods that can continuously quantify tremor classes in a desktop setting without compromising the privacy of the enrolled subjects, such as digital handwriting analysis with an iPad (Touchscreen) and Apple Pencil [10,11,23,24], as well as Doppler mm-Wave biosensors with the X- (10.525 GHZ), K- (24 GHz), and W-band (76-81 GHz) radars [7,30,48,49]. Digital handwriting analysis was a non-invasive and easy-to-use tool that could be utilized in both hospital and home settings. In contrast to conventional paper-based handwriting tests, digital methods provided quantifiable measurements on pattern shapes, writing speeds, stroke pressures, and tremor frequencies. Refers to various predefined geometric patterns, such as spirals and straight lines (horizontal or vertical) [10,11], the aforementioned records could be transformed into a polar representation, including radius, angle, and tremor oscillations in a curved trajectory, to quantify different hand movement disorders for PD screening or early diagnosis. Then, ML- or DL- based classifiers, such as nonlinear SVM [10], GRNN

 doi:10.20944/preprints202604.2032.v1

(General Regression Neural Network) [11], VGGs [23], and 2D CNN [24], were applied for automatically analyzed the aforementioned feature patterns for subsequent recognition in PD screening, which indicted an mean accuracy (mean hit rate) of > 90% for the intended purpose, as seen the experiment results in Table 5. However, its sensing manner was assistive tool dependency which required specialized hardware to access these digital handwritten patterns. Thus, older subjects or those unfamiliar with digital assistive tool might have difficulty to perform the handwriting tests. In addition, variations in individual handwriting habits, stress levels, and medication intake, there was no gold standardized protocol for tremor quantification, potentially affecting the reliability of tremor analysis.

The mm-Wave sensing with FMCW were also non-contact, privacy-preserving, and real-time processing methods for continuous monitoring in ULT quantification [7,30,49] and gesture recognition (wipe, swing, push, invalid, and circle) applications [48]. Its method was less affected by environmental factors compared to cameras or optical techniques. While lower-frequency radar bands, such as X and K bands, provided extended sensing ranges and balanced resolution for general hand motion tracking and tremor detection, their limited resolution reduced the sensitivity to mDE, thereby requiring a trade-off between sensing ranges and resolutions. For example, using X-band (10.525 GHz) mm-Wave sensing with FMCW method, Reference [7] demonstrated good resolution at a measurement distance of 0.30 ± 0.1 m for time-domain parametric feature extraction. Three quantitative features, such as ZC, WAMP, and WL, showed a positive correlation (mean coefficient of determination, $R^2 > 0.85$) with different ULT classes, which were effective in quantifying normal conditions, Myorhythmia and Holmes tremors (< 4.0 Hz), and PDT (4.0–8.0 Hz). The Reference [30] also demonstrated the use of a W-band (77.0 GHz) FMCW radar sensor for the PDT and ET quantification. The tremor frequencies and amplitudes were extracted from reflected electromagnetic signals. The linear regression method was used to analyze the feature parameters obtained from the contactless and ground truth (accelerometer and gyroscope) sensing methods. Thus, compared to the ground truth method, the contactless mm-Wave sensing method demonstrated a high level of agreement ($R^2 > 0.97$), indicating strong correlation for continuous monitoring to predict the level of tremor severity.

Therefore, the higher-frequency W-band radar had higher resolution mDE detection for maintaining sufficient precision in fine tremor quantification. In our study, we proposed the WVD- and SPWVD-based feature extraction methods [40–42] to enhance the mD signatures for improving recognition accuracy. For large hand motions, in Reference [48], the K-band mm-Wave radar had a balance between resolution, sensing range, and penetration for gesture recognition. The gestures' 2D time-feature maps with a lightweight CNN was used to classify different hand gestures, achieved a recognition accuracy of 99.60% for five gesture classes, including Wipe, Swing, Push, Invalid, and Circle. In our study, we proposed "WVD + 2D CNN" and "SPWVD + 2D CNN" based classifiers for automatic ULT classification, obtained promising average accuracies of 93.81 ± 1.88% and 95.89 ± 0.62% and average F1 scores of 0.9379 ± 0.1900 and 0.9588 ± 0.0060 for the intended purpose, respectively, as seen in Table 5. The W-band mm-Wave radar offered superior resolution compared to X- and K-band those in tremor motions detection and detailed feature extraction. Hence, the proposed short-range and contactless sensing tool and classifier model had promising performances for real-time tremors monitoring and ULT classification.

Table 5. Comparisons of different non-contact and short range sensing methods.

Sensing Method	Reference	Classification Method	Experimental Results
Digital Handwriting Method	[10]	Nonlinear SVM	Mean Hit Rate (%) = 92.13% for PD Screening
	[11]	GRNN	Mean Hit Rate (%) = 98.93% for PD Screening

 doi:10.20944/preprints202604.2032.v1

	[24]	VGGs	Mean Accuracy (%) = 93.3% for PD Detection
	[24]	2D CNN	Mean Accuracy (%) = 93.3% for Early PD Diagnosis
X-band (10.525 GHz) Doppler mm-Wave Sensing with FMCW Short Range (0.2–0.4 m)	[7]	Linear Regression Method and Color Visual Representation	ULT Quantification: PDT (4–8 Hz), Myorhythmia and Holmes Tremors (< 4Hz), and Normal Condition ZC: R^2= 0.8949, WAMP: R^2= 0.8918, WL: R^2= 0.8553 for ULT Quantification
K-band (24 GHz) Doppler mm-Wave Sensing with FMCW Non-contact Sensing in Short Range (0.7 m)	[48]	Lightweight CNN for 2D images processing and classification	Gesture Recognition: Wipe, Swing, Push, Invalid, and Circle Recognition Accuracy (%) = 99.60% for all Gesture Types
W-band (77 GHz) Doppler mm-Wave Sensing with FMCW Non-contact Sensing in Short Range (3.0–6.0 m)	[30]	Linear Regression Method Correlation Plots for all Trials Tremor Frequency and Amplitude Parameters	**P**arkinson's and Essential Tremor Quantification: Action, Posture, Rest Upper Limb, and Rest Lower Limb Tremors $R^2 > 0.966$ for both Frequency and Amplitude. Parameters (Mean Values: 0.14 Hz and 0.03 cm)
Proposed Method Non-contact Sensing in Short Range (0.5–1.0 m)	—	WVD + 2D CNN SPWVD + 2D CNN	ULT Classification: • WVD + 2D CNN: Average Accuracy (%) = 93.81 ± 1.88%, Average F1 score = 0.9379 ± 0.1900 for ULT Classification • SPWVD + 2D CNN: Average Accuracy (%) = 95.89 ± 0.62%, Average F1 score = 0.9588 ± 0.0060 for ULT Classification

4. Conclusions

Clinical assessments commonly relied on the MDS- UPDRS and Health-Related Quality of Life (HRQOL) [33,34] questionnaires for face-to-face evaluations. During PD examinations, physicians also observed abnormal symptoms based on the PD patients' motor function, coordination, and balance, including whether the upper limb exhibited RT, muscle rigidity and bradykinesia during

 doi:10.20944/preprints202604.2032.v1

body movement, and the voice became softer. These symptoms would manifest in the upper or lower limbs, body, and vocal characteristics. However, these examination manners required significant time and human resources for questioning and scoring (from 0 to 4 scores). This traditional assessment method lacked scientific data quantification, automated detection, repeatability, and personalized application, posing limitations for standardized evaluations. Hence, we had proposed a short- range and contactless sensing method for ULT classification by using W-band mm-Wave biosensor, including three ranges of tremor frequencies and possible ULT classes, referring to low-frequency tremors (< 4.0 Hz), PDT (4.0-7.0 Hz), and ET (> 7.0 Hz). The WVD and SPWVD methods were employed to enhance the mD feature resolution, providing a more refined and color- encoded feature representations for pattern recognition tasks. Considered trade-off among resolution, sensing range, and classifier model, we suggested the suitable measurement site at location 0.5 m and designed the "SPWVD + 2D CNN" based classifier which could effectively and reliably screen ULT classes. Our HW-SW device could be easily implemented on desktop assistive tool for individualized assessment of tremor progression, enabling self-care and medication adjustment requirements. However, the W-band mm-Wave sensing tools demonstrate high potential in a university laboratory setting; nonetheless, they remain in the research phase, and further clinical trials with PD patients are necessary to establish standardized protocols for ULT assessment in future works.

Author Contributions: Conceptualization: Chia-Hung Lin and Pi-Yun Chen; Methodology: Chia-Hung Lin and Pi-Yun Chen; Software: Chun-Yu Lin and Ping-Tzan Huang; Validation: Neng-Sheng Pai and Chao-Lin Kuo; Formal Analysis: Chia-Hung Lin and Pi-Yun Chen; Investigation: Chien-Ming Li; Data Curation: Chien-Ming Li, Chun-Yu Lin, and Ping-Tzan Huang; Writing—Original Draft Preparation: Chia-Hung Lin and Pi-Yun Chen; Writing—Review and Editing: Chia-Hung Lin and Pi-Yun Chen; Visualization; Neng- Sheng Pai, Chao-Lin Kuo, and Chien-Ming Li; Supervision: Chia-Hung Lin; Project Administration: Chia- Hung Lin and Pi-Yun Chen; Funding Acquisition: Chia-Hung Lin. All authors have read and agreed to the published version of the manuscript.

Funding: This work was supported by the National Science and Technology Council (NSTC), Taiwan, under contract number: ***NSTC 114-2221-E-167-006***, duration: August 1, 2025—July 31, 2026.

Institutional Review Board Statement: This work was approved by the hospital research ethics committee and the Institutional Review Board (IRB), under contract number: *SCMH_ IRB No: 1130103*, January 04, 2024—January 03, 2025, Show Chwan Memorial Hospital, Changhua, Taiwan.

Informed Consent Statement: Not applicable.

Data Availability Statement: The dataset can be shared with the corresponding author upon request with justification.

Conflicts of Interest Statement: The authors declare no conflict of interest.

References

1. Yoshio Tahara, "Cardiopulmonary resuscitation in a super-aging society–is there an age limit for cardiopulmonary resuscitation?, "Circulation Journal Official Journal of the Japanese Circulation Society, vol. 80, 2016, pp. 1102-1103, **http://www.j-circ.or.jp.**
2. Kozo Nakamura, "A "super-aged" society and the "locomotive syndrome", "J. Orthop. Sci., vol. 13, no. 1, 2008, pp. 1-2, **doi: 10.1007/s00776-007-1202-6.**
3. T. B. Stoker and J. C. Greenl, Parkinson's disease: pathogenesis and clinical aspects, Brisbane (AU): Codon Publications, Australia, 2018,**DOI:http://dx.doi.org/10.15586/ codonpublications.parkinsonsdisease.2018**
4. Parkinson's Foundation, Statistics : Get informed about Parkinson's disease with these key numbers., [online 2025] available: **https:// www. parkinson.org/understanding-parkinsons/statistics.**
5. Elena Cecilia Rosca, Raluca Tudor, Amalia Cornea, and Mihaela Simu, "Parkinson's disease in Romania: A scoping review protocol, "Brain Sci., vol. 11, no. 2, 2021, pp. 1-5, **doi: 10.3390/brainsci11020251**.

 doi:10.20944/preprints202604.2032.v1

6. Soumya Sharma and Sanjay Pandey, "Approach to a tremor patient, "Annals of Indian Academy of Neurology, vol. 19, no. 4, 2016, pp.433-443, **doi: 10.4103/0972-2327.194409**.
7. Chia-Hung Lin, Jian-Xing Wu, Jin-Chyr Hsu, Pi-Yun Chen, Neng-Sheng Pai, and Hsiang-Yueh Lai, "Tremor class scaling for Parkinson disease patients using an array X-band microwave Doppler based upper limb movement quantizer, "IEEE Sensors Journal, vol. 21, no. 19,2021, pp. 21473-21485, **doi: 10.1109/JSEN.2021.3103803**.
8. Jun Hua Bowen Lim, Victoria Newgreen, and Paul Kopanidis, "Tremor: A systematic approach, "Clinical, vol. 53, no. 12, Suppl., 2024,pp. S61-S67, **doi: 10.31128/AJGP-02-24-7151**.
9. Jaron van de Wardt, A. M. Madelein van der Stouwe, Michiel Dirkx, Jan Willem J. Elting , and Bart Post, "Systematic Clinical Approachfor diagnosing upper limb tremor, "J. Neurol Neurosurg Psychiatry, vol. 91, 2020, pp. 822–830, **doi:10.1136/jnnp-2019-322676**.
10. Tsung-Lung Yang, Ping-Ju Kan, Chia-Hung Lin, Hsin-Yu Lin, Wei- Ling Chen, and Her-Terng Yau, "Using polar expression features and nonlinear machine learning classifier for automated Parkinson's disease screening, "IEEE Sensors Journal, vol. 20, no. 1, 2020, pp.501-514, **doi: 10.1109/JSEN.2019.2940694**.
11. Tsung-Lung Yang, Chia-Hung Lin, Wei-Ling Chen, Hsin-Yu Lin, Chen-San Su, and Chih-Kuang Liang, "Hash transformation and machine learning-based decision-making classifier improved the accuracy rate of automated Parkinson's disease screening, "IEEE Transactions onNeural Systems and Rehabilitation Engineering, vol. 28, no. 1, 2020, pp. 72-82, **doi: 10.1109/TNSRE.2019.2950143.**
12. T. Sridhar Reddy, N. Leelavathy, B. Gnaneswarara Rao, P. Kavya Keerthi, I. Kumar Chandra, and T. Rambabu, "Speech insight: Parkinson's disease diagnosis using random forest classifier, "2025 6th International Conference on Mobile Computing and Sustainable Informatics (ICMCSI), Goathgaun, Nepal, 2025, pp. 1254-1260, **doi: 10.1109/ICMCSI64620.2025.10883452**.
13. Al Jizani, Mohammed Kadhim Salman, and Grigore Stamatescu, "Daily monitoring of speech impairment for early Parkinson's disease Detection, "The 12th IEEE International Conference on Intelligent Data Acquisition and Advanced Computing Systems: Technology and Applications 7-9 September, 2023, Dortmund, Germany, 2023, pp. 1049-1053, **doi: 10.1109/IDAACS58523.2023.10348855**.
14. Nader Naghavi and Eric Wade, "Prediction of freezing of gait in Parkinson's disease using statistical inference and Lower–Limb acceleration data, "IEEE Transactions on Neural Systems and Rehabilitation Engineering, vol. 27, no. 5, 2019, pp. 947-955, **doi: 10.1109/TNSRE.2019.2910165**.
15. Bryan T. Cole, Serge H. Roy, and S. Hamid Nawab, "Detecting freezing-of-gait during unscripted and unconstrained activity, "2011 Annual International Conference of the IEEE Engineering in Medicine and Biology Society, Boston, MA, USA, 2011, **doi: 10.1109/ IEMBS.2011.6091367**
16. Salim Lahmiri, "Gait Nonlinear Patterns Related to Parkinson's Disease and Age, "IEEE Transactions on Instrumentation and Measurement, vol. 68, no. 7, 2019, pp. 2545-2551, **doi: 10.1109/TIM.2018.2866316.**
17. Ali Saad, Iyad Zaarour, Dimitri Lefebvre, François Guerin, Paul Bejjani, and Mohammad Ayache, "About detection and diagnosis of Freezing of Gait, "2013 2nd International Conference on Advances in Biomedical Engineering, Tripoli, Lebanon, 2013, **doi: 10.1109/ICABME.2013.6648861.**
18. Bhavana C., Jishu Gopal, Raghavendra P., K. M. Vanitha, and Viswanath Talasila, "Technique of measurement for Parkinson's tremo high-lighting advantages of embedded IMU over EMG, "2016 International Conference on Recent Trends in Information Technology,Chennai, India, 2016, **doi: 10.1109/ICRTIT.2016.7569560.**
19. Alexandros Papadopoulos, Konstantinos Kyritsis, Lisa Klingelhoefer, Sevasti Bostanjopoulou, K. Ray Chaudhuri, and Anastasios Delopoulo, "Detecting Parkinsonian tremor from IMU data collected in-the-wild using deep multiple-instance learning, "IEEE Journal of Biomedical and Health Informatics, vol. 24, no. 9, 2020, pp. 2559-2569, **doi: 10.1109/JBHI.2019.2961748.**
20. Beatriz S. Arruda, Carolina Reis, James J. Sermon, Alek Pogosyan, Peter Brown, and Hayriye Cagnan, "Identifying and modulating distinct tremor states through peripheral nerve stimulation in Parkinsonian rest tremor, "Journal of NeuroEngineering and Rehabilitation, vol. 18, no. 179, 2021, pp. 1-15, **doi: https://doi.org/10.1186/s12984-021-00973-6.**
21. Bhavana C., Jishu Gopal, Raghavendra P., K. M. Vanitha, and Viswanath Talasila, "Technique of measurement for Parkinson's tremor high-lighting advantages of embedded IMU over EMG, "2016

 doi:10.20944/preprints202604.2032.v1

International Conference on Recent Trends in Information Technology, Chennai, India, 2016, **doi 10.1109/ICRTIT.2016.7569560.**

22. M. Shamim Hossain and Mohammad Shorfuzzaman, "Meta Parkinson: A cyber-physical deep meta-learning framework for n-shot diagnosis and monitoring of Parkinson's patients, "IEEE Systems Journal, vol. 17, no. 4, 2023, pp. 5251–5260, **doi: 10.1109/JSYST.2023.3308333.**
23. Nabil Daiyan and Md Rakibul Haque, "Exploring the efficacy of modified transfer learning in identifying Parkinson's disease through drawn image patterns, "2024 2nd International Conference on Information and Communication Technology (ICICT), **doi: 10.1109/ICICT64387.2024.10839723**
24. Nivedita Manohara Mathkunti, Shanta Rangaswamy, Sainath Somappa Yalavigi, Samarth Siddappa Shellikeri, and Someshwar Sanjay Magadum, "Early diagnosis of Parkinson's disease using deep learning and average voting classifier, "2024 Second International Conference on Data Science and Information System (ICDSIS), Hassan, India, 2024, pp. 1-6, **doi: 10.1109/ICDSIS61070.2024.10594705.**
25. Kun Hu, Zhiyong Wang, Wei Wang, Kaylena A. Ehgoetz Martens, Liang Wang, Tieniu Tan, Simon J. G. Lewis, and David Dagan Feng, "Graph sequence recurrent neural network for vision-based freezing of gait detection, "IEEE Transactions on Image Processing, vol. 29, 2020, pp. 1890–1901, **doi: 10.1109/TIP.2019.2946469.**
26. A. M. Ardi Handojoseno, James M. Shine, Tuan N. Nguyen, Yvonne Tran, Simon J. G. Lewis, and Hung T. Nguyen, "Analysis and prediction of the freezing of gait using EEG brain dynamics, "IEEE Transactions on Neural Systems and Rehabilitation Engineering, vol. 23, no. 5, 2015, pp. 887-896, **doi: 10.1109/TNSRE.2014.2381254.**
27. Isabelle Killane, Glen Browett, and Richard B. Reilly, "Measurement of attention during movement: Acquisition of ambulatory EEG and cognitive performance from healthy young adults, "2013 35th Annual International Conference of the IEEE Engineering in Medicine and Biology Society (EMBC), Osaka, Japan, 2013, **doi: 10.1109/EMBC.2013.6611018.**
28. Malcolm Ng Mou Kehn, Eva Rajo-Iglesias, and Tien-Chen Yang, "W-band 76–81 GHz millimeter-wave comb-line array for automotive short range radar, "Radio Science, vol. 57, no. 4, 2022, pp. 1-14, **doi: 10.1029/2021RS007407.**
29. Gaopeng Tang, Tongning Wu, and Congsheng Li, "Dynamic gesture recognition based on FMCW millimeter wave radar: Review of meth odologies and results, "Sensors, vol. 23, no. 17, 2023, pp. 1-19, **https://doi.org/10.3390/s23177478.**
30. Nazia Gillani, Tughrul Arslan, and Gillian Mead, "An unobtrusive method for remote quantification of Parkinson's and essential tremor using mm-Wave sensing, "IEEE Sensors Journal, vol. 23, no. 9, 2023, pp. 10118-10131, **doi: 10.1109/JSEN.2023.3261111.**
31. Omid Bazgir, Seyed Amir Hassan Habibi, Lorenzo Palma, Paola Pierleoni, and Saba Nafees, "A classification system for assessment and home monitoring of tremor in patients with Parkinson's disease, "J Med Signals Sens., vol. 8, no. 2, 2018, pp. 65–72, **doi: PMID: 29928630.**
32. Jonathan A. Sisti, Brandon Christophe, Audrey Rakovich Seville, Andrew L. A. Garton, Vivek P. Gupta, Alexander J. Bandin, Qiping Yu, and Seth L. Pullman, "Computerized spiral analysis using the iPad, "Journal of Neuroscience Methods, vol. 275, 2017, pp. 50-54, **doi: 10.1016/j.jneumeth.2016.11.004.**
33. Mayo Clinic Health Letter, Parkinson's disease, 1998-2025, available: https://www.mayoclinic.org/disease-conditions/parkinsons-disease/ symptoms/symptoms-cause/syc-20376055.
34. Claudia Ramaker, Johan Marinus, Anne Margarethe Stiggelbout, and Bob Johannes van Hilten, "Systematic evaluation of rating scales for impairment and disability in Parkinson's disease, "Movement Disorders, vol. 17, no. 5, 2002, pp. 867-876, **doi: 10.1002/mds.10248.**
35. Tiange Li, Guangyang Wan, Linsheng Liu, Tong Zhu, and Peng Wang, "ECG signal detection method based on millimeter wave rdar, " 2022 IEEE 2nd International Conference on Information Communication and Software Engineering (ICICSE), Chongqing, China, 2022, **doi: 10.1109/ICICSE55337.2022.9828872.**
36. Yuchen Li, Keke Zheng, and Changzhan Gu, "A fast and efficient FMCW radar phase extraction technique at ultra- narrow range for vital sign Detection, "2024 IEEE/MTT-S International Microwave Symposium—IMS 2024, Washington, DC, USA, 2024, **doi: 10. 1109/ IMS5.2024.10600232.**

37. Qin Chen, Zheng Zhou, Zongyong Cui, YuTian , and Zongjie Cao, "MMHTSR: In-Air Handwriting Trajectory Sensing and Reconstruction Based on mmWave Radar, "IEEE Internet of Things Journal, vol. 11, no. 6, 2024, pp. 10069-10083, **doi: 0.1109/ JIOT.2023.3325258.**
38. Pi-Yun Chen, Hsu-Yung Lin, Zi-Heng Zhong, Neng-Sheng Pai, Chien-Ming Li, and Chia-Hung Lin, "Contactless and short-range vital signs detection with Doppler radar millimeter-wave (76-81 GHz) sensing firmware, "IET Healthcare Technology Letters, vol. 11, no. 6, , pp. 427-436, **https://doi.org/10.1049/htl2.12075.**
39. Pi-Yun Chen, Yu-Cheng Cheng, Zi-Heng Zhong, Feng-Zhou Zhang, Neng-Sheng Pai, Chien-Ming Li, and Chia-Hung Lin, "Information security and artificial intelligence—assisted diagnosis in an internet of medical thing system (IoMTS), "IEEE Access, vol. 12, 2024, pp.-9775, **doi: 10.1109/ACCESS.2024.3351373**.
40. Kewei Cai, Wenping Cao, Lassi Aarniovuori, Hongshuai Pang, Yuanshan Lin, and Guofeng Li, "Classification of power quality disturbances using Wigner-Ville distribution and deep convolutional neural networks, "IEEE Access, vol. 7, 2019, pp. 119099–119109, **doi:109/ACCESS.2019.2937193**
41. Manish Kalra, Satish Kumar, and Bhargab Das, "Moving ground target detection wth seismic signal using smooth pseudo Wigner–Ville Distribution, "IEEE Transactions on Instrumentation and Measurement, vol. 69, no. 6, 2020, pp. 3896-3906, **doi: 10.1109/TIM.2019.2932176.**
42. Xing-Jian Wang, Ya-Juan Xue, Wen Zhou, and Jun-Song Luo, "Spectral decomposition of seismic data with variational mode decomposition-based Wigner–Ville distribution, "IEEE Journal of Selected Topics in Applied Earth Observations and Remote Sensing, vol. 12, no.11, 2019, pp. 4672–4683, **doi: 10.1109/JSTARS.2019.2953341.**
43. Feng-Zhou Zhang, Chia-Hung Lin, Pi-Yun Chen, Neng- Sheng Pai, Chunmin Su, Ching-Chou Pai, and Hui-Wen Ho, "Number of convolution layers and convolution kernel determination and validation for multilayer convolutional neural network: case study in breast lesionscreening of mammographic images, " Processes, vol. 10, no. 9, 2022, pp. 1-19, **https://doi.org/10.3390/pr10091867.**
44. Yaoshiang Ho and Samuel Wookey, "The real-world-weight cross- entropy loss function: modeling the costs of mislabeling, "IEEE Access,vol. 8, 2019, pp. 4806-4813, **doi: 10.1109/ACCESS.2019.2962617.**
45. R. Mahima, M. Maheswari, S. Roshana, E. Priyanka, Neha Mohanan, and N. Nandhini, "A comparative analysis of the most commonly used activation functions in deep neural network, "2023 4th International Conference on Electronics and Sustainable Communication Systems (ICESC), Coimbatore, India, 2023, pp. 1334-1339, **doi: 10.1109/ICESC57686.2023.10193390.**
46. Y. Zhang, D. S. Park, W. Han, J. Qin, A. Gulati, J. Shor, A. Jansen, Y. Xu, Y. Huang, S. Wang, et al., "BigSSL: Exploring the frontier of large-scale semi-supervised learning for automatic speech recognition, "IEEE J. Sel. Top. Signal Process, vol. 16, 2022, pp. 1519–1532, **https://doi.org/10.48550/arXiv.2109.13226.**
47. Fen Li, Ming Liu, Yuejin Zhao, Lingqin Kong, Liquan Dong, Xiaohua Liu, and Mei Hu, "Feature extraction and classification of heart sound using 1D convolutional neural network, "EURASIP Journal on Advances in Signal Processing, vol. 59, 2019, pp. 1-11, **https:// doi.org/10.1186/s13634-019-0651-3.**
48. Jiayu Chen, Xinhuai Wang, Yin Xu, Wen Wang, Ye Peng, Ming Fu, and Chunyan Qiu, "Gesture recognition using MIMO radar Point clouds with targeted signal processing for resource-limited platforms, "IEEE Sensors Journal (Early Access), October 2024, pp. 1-20, **doi: 10.1109/JSEN.2024.3481964.**
49. G. Blumrosen, M. Uziel, B. Rubinsky, and D. Porrat, "Non-contact UWB radar technology to assess tremor, "IFMBE Proceedings of XII Mediterranean Conference on Medical and Biological Engineering and Computing, vol 29, 2010, pp. 490-493, Springer, Berlin, Heidel berg, **doi: https://doi.org/10.1007/978-3-642-13039-7_123.**
50. Chun-Yu Lin, Design and evaluation of a non-contact tremor detection system for Parkinson's disease using millimeter-Wave echo features and deep learning, Thesis for Degree of Master, Department of Electrical Engineering, National Chin-Yi University of Technology, July, 2025.